# Investigation of Mixing in a Turbofan Exhaust Duct, Part I: Analysis and Computational Procedure

J. P. Kreskovsky,* W. R. Briley,† and H. McDonald‡
*Scientific Research Associates, Inc., Glastonbury, Connecticut*

**An analysis and computational procedure are described for computing three-dimensional, turbulent, subsonic flow in turbofan lobe mixer exhaust nozzles. The analysis is designed to treat the large secondary flows that are believed to occur within mixing ducts and to affect mixer performance. The solution procedure is first tested for a two-dimensional (axisymmetric) coaxial jet flow measured by Forstall and Shapiro. Very good agreement is obtained for both centerline velocity decay and jet spreading rate. The ability of the present procedure to obtain predictions for thrust gains and total pressure losses as a result of the mixing process is then demonstrated for a lobe mixer geometry. Flow both with and without inlet secondary vorticity is considered in calculations performed in collaboration with Povinelli and Anderson, and it is found that secondary flow associated with inlet vorticity exerts a significant influence on the mixing process. Finally, calculations performed with a two-equation turbulence model and with a much simpler wake model indicate that the predictions are not sensitive to the differences between these two turbulence models. Further extensive computational results, validation, and data comparisons are given in a companion paper.**

## Introduction

TURBOFAN engines may use a device known as a lobe mixer to mix the hot turbine exhaust with the cold fan flow and provide a more uniform total energy distribution in the exhaust gases. This may lead to an increase in thrust when these gases are expanded through the exhaust nozzle. Although this method for increasing performance has been known for some time, the details of the mixing process within the mixing duct and exhaust nozzle have not been well understood, and analytical methods for predicting these flows have not been available. As a result, designers have had to rely upon costly and time-consuming experiments, often with measurements taken only at the exhaust nozzle exit, to determine optimum mixer configurations. Obviously, a method capable of accurately predicting mixer flows in detail would be useful as a design aid. This has led to the development of analytical methods,[1,2] one of which is described here, for making detailed predictions of the three-dimensional mixing process within the mixing duct and exhaust nozzle downstream of the lobe mixer exit plane.

Numerical predictions for flow in a turbofan exhaust duct with lobe mixing have also been obtained in a previous study by Birch et al.[2] They employed a modification (for application to internal mixing flows) of the calculation procedure of Patankar and Spalding[3] for three-dimensional "parabolic" flows with negligible streamwise diffusion. Birch et al.[2] compared predictions using this calculation procedure with experimental measurements and obtained encouraging results for three different mixer flows.

The present study considers an alternative method based on the primary/secondary velocity decomposition approach of Briley and McDonald[4] for application to viscous subsonic flow in smoothly curved geometries. The axial or primary flow is governed by an approximate momentum equation in which axial pressure gradients from an a priori inviscid axisymmetric potential flow for the mixing duct geometry in question are imposed and then corrected by a mean (viscous) pressure drop. The potential flow satisfies an elliptic equation, is subject to downstream boundary conditions, and is the sole method of accounting for transverse variations in the streamwise pressure gradient within the mixing duct. Very substantial secondary flows (on the order of 20-30% of the axial velocity) are anticipated in the mixing duct, because of the radial deflection of the flow within the mixer lobes and because of the upstream viscous flow development. The large transverse velocities originating in the mixer lobes are represented in the present starting condition at the entrance to the mixing duct. The secondary flow development within the mixing duct is treated by the solution of an approximate equation governing the growth of streamwise vorticity, including viscous effects. Conservation of mass is ensured by introducing scalar and vector surface potentials for the transverse velocity, and thermal transport is governed by an energy equation. The present approximating equations apply in both viscous and inviscid regions and account for secondary flows, turbulence, heat transfer, total pressure distortion, and internal flow blockage and losses. No assumption of small cross-flow velocity is required. If reversal of the primary velocity occurs, the present method is not applicable unless further approximations are introduced. The method is also restricted to cross-sectionally averaged Mach numbers less than 1.0, although the local Mach number may exceed unity.

## Analysis

### Geometry and Coordinate System

The analysis is based on approximations made relative to an axisymmetric orthogonal coordinate system developed for the geometry in question (cf. Figs. 1 and 2). As shown in Fig. 1, the lobe mixer directs the cold fan flow and hot turbine exhaust so as to enhance the mixing of the two streams. The present analysis treats the flow within the mixing duct downstream of the lobe mixer. The coordinate system (Fig. 2) is chosen such that the streamwise or marching direction is approximately aligned with a known inviscid primary flow direction as defined by a potential flow solution in the given geometry. The area immediately downstream of the nozzle plug is faired in with an assumed streamline to model the expected reversed flow region in a manner that allows solution by forward marching. The flow area thus excluded from consideration is very small, and this treatment is not believed to introduce significant error. As a result of the choice of

Received Dec. 21, 1981; revision received May 12, 1983. Copyright © 1983 by J. P. Kreskovsky. Published by the American Institute of Aeronautics and Astronautics with permission.

*Senior Research Scientist.
†Vice President. Member AIAA.
‡President. Member AIAA.

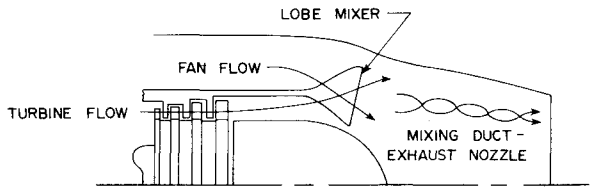


**Fig. 1 Schematic representation of flow through a turbofan lobe mixer.**

coordinates, transverse computational planes are normal to the bounding surfaces.

The equations are written in orthogonal coordinates $x_1$, $x_2$, and $x_3$ with unit vectors $\hat{i}_1$, $\hat{i}_2$, and $\hat{i}_3$ constructed to fit the flow passage boundaries as shown in Fig. 2. In this system, $\hat{i}_1$ is normal to the transverse surfaces, $\hat{i}_2$ is in the direction of the principal curvature of the $x_1$ coordinate, and $\hat{i}_3$ is in the azimuthal direction. Metric coefficients $h_1$, $h_2$, and $h_3$ are defined such that the incremental distance $s$ is determined by $(\delta s)^2 = (h_1 \delta x_1)^2 + (h_2 \delta x_2)^2 + (h_3 \delta x_3)^2$. In planes of constant azimuth, $x_3$, orthogonal streamlines and velocity potential lines from a two-dimensional planar incompressible potential flow analysis developed by Anderson[5] are utilized as the $x_1$-$x_2$ coordinates, respectively. This $x_1$-$x_2$ coordinate system is rotated about the mixing duct centerline to form an axisymmetric coordinate system. The $x_1$ coordinate is identified as the primary flow or streamwise coordinate, and the $x_2$-$x_3$ surfaces define the transverse secondary flow surfaces at a given $x_1$ location.

### Primary/Secondary Velocity Decomposition

The analysis is based on decomposition of the velocity vector $\boldsymbol{U}$ into primary and secondary flow components $\boldsymbol{U}_p$ and $\boldsymbol{U}_s$, respectively. This decomposition is expressed as

$$\boldsymbol{U} = \boldsymbol{U}_p + \boldsymbol{U}_s \tag{1}$$

The primary flow component is written as

$$\boldsymbol{U}_p = \hat{i}_1 u_p \tag{2}$$

The secondary flow velocity $\boldsymbol{U}_s$ is constructed to lie in the transverse coordinate surface and is determined from scalar and vector surface potentials $\phi$ and $\psi$, respectively. If $\rho$ is the fluid density, then $\boldsymbol{U}_s$ is defined by

$$\boldsymbol{U}_s \equiv \nabla_s \phi + (1/\rho) \nabla \times \hat{i}_1 \psi \tag{3}$$

where $\nabla_s$ is a surface gradient operator defined as

$$\nabla_s \equiv \nabla - \hat{i}_1 (\hat{i}_1 \cdot \nabla) \tag{4}$$

Equation (3) is sufficiently general to permit both rotational and irrotational secondary flows and leads to equations governing $\boldsymbol{U}_s$, which are elliptic in *transverse* coordinate surfaces and are, therefore, solvable within a forward-marching context. The overall velocity decomposition may thus be written

$$\boldsymbol{U} = \hat{i}_1 u_p + \nabla_s \phi + (1/\rho) \nabla \times \hat{i}_1 \psi \tag{5}$$

### Governing Equations

Approximate equations governing the primary and secondary flow development are derived utilizing assumptions that permit forward-marching solution. The terms representing diffusion normal to the transverse coordinate surfaces are neglected. The axial component of velocity is governed by a streamwise momentum equation in which the axial pressure gradients determined from the inviscid potential velocity $\boldsymbol{U}_I$ are imposed, and an additional mean viscous pressure drop is introduced to ensure that global continuity of the mass flux is maintained. Secondary flow velocities lie in the transverse coordinate surfaces and are determined by solution of scalar and vector surface potentials in conjunction with a streamwise vorticity equation. The governing equations may be grouped into three subsets: 1) those governing the primary flow and thermal energy, 2) those governing the secondary flow development, and 3) turbulence model equations. These equations are given here in vector form and are given for general orthogonal coordinates in Ref. 1.

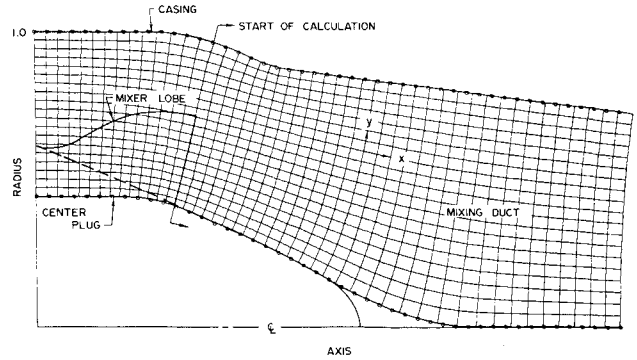


**Fig. 2 High-bypass lobe mixer geometry and potential flow coordinate system.**

*Primary Flow Equations*

The primary flow equations consist of the streamwise momentum equation, a thermal energy equation, an equation of state, and an integral continuity equation. These equations are given, respectively, by

$$\hat{i}_1 \cdot [(\boldsymbol{U} \cdot \nabla) \boldsymbol{U} + (\nabla p)/\rho] = \hat{i}_1 \cdot \boldsymbol{F} \tag{6}$$

$$\rho \boldsymbol{U} \cdot \nabla E = \nabla \cdot k \nabla T + \boldsymbol{U} \cdot \boldsymbol{F} + \Phi \tag{7}$$

$$P = \rho R T = \rho R (E - \tfrac{1}{2} \boldsymbol{U} \cdot \boldsymbol{U}) / C_p \tag{8}$$

and

$$\int_A \hat{i}_1 \cdot \rho \boldsymbol{U} \mathrm{d}A = \text{const} \tag{9}$$

In Eqs. (6-9) $p$ is the pressure, $\rho \boldsymbol{F}$ the force due to viscous (and turbulent) stress, $E$ the total enthalpy, $T$ the temperature, $k$ the thermal conductivity, $\Phi$ the dissipation function, $C_p$ the specific heat, $R$ the gas constant, and $A$ the cross-sectional area of the mixing duct. Terms in $\boldsymbol{F}$ representing streamwise diffusion and the streamwise diffusion of thermal energy must be neglected to permit forward-marching solution. The actual approximations used are given subsequently. In addition, the axial pressure gradient term in Eq. (6) must be approximated, and $p$ is thus replaced by the sum of an imposed pressure $p_I$ determined from the axisymmetric potential velocity $\boldsymbol{U}_I$ and a mean viscous pressure correction $p_v$ that depends only on $x_1$.

The pressure gradient term is thus approximated by

$$\hat{i}_1 \cdot \nabla p \doteq \hat{i}_1 \cdot [\nabla p_v(x_1) - \rho \nabla (\boldsymbol{U}_I \cdot \boldsymbol{U}_I)/2] \tag{10}$$

The viscous correction $p_v$ is determined to ensure that Eq. (9) is satisfied.

*Secondary Flow Equations*

The equations governing the secondary flow development consist of a streamwise vorticity equation and equations for the scalar and vector surface potentials. The equation

governing $\Omega_s$ along a streamline is given by Lakshminarayana and Horlock[6] and may be written as

$$\frac{\partial}{\partial s}\left(\frac{\Omega_s}{\rho q}\right)=\frac{2\Omega_n}{\rho q R}-\frac{1}{\rho q^2}\hat{s}\cdot\nabla\times\frac{1}{\rho}\nabla p+\frac{1}{\rho q^2}\hat{s}\cdot\boldsymbol{G} \tag{11}$$

where $q$ is the velocity magnitude, $\hat{s}$ the unit vector along a streamline, $s$ the distance along a streamline, $\Omega_n$ the vorticity in the direction of the unit principal normal vector $\hat{n}$ of the streamlines, for which $R$ is the principal radius of curvature, and $\boldsymbol{G}\equiv\nabla\times\boldsymbol{F}$. $R$ and $\hat{n}$ are related by the Frenet formula $n/R=\partial\hat{s}/\partial s=\hat{s}\cdot\nabla\hat{s}$.

Since the coordinate system used here is approximately aligned with the flow direction, an approximate equation for $\Omega$ can be derived from Eq. (11) by replacing $\hat{s}$ with $\hat{i}$, as follows:

$$\frac{\Omega_s}{q}=\frac{\hat{s}\cdot\boldsymbol{\Omega}}{\hat{s}\cdot\boldsymbol{U}}\doteq\frac{\hat{i}_1\cdot\boldsymbol{\Omega}}{\hat{i}_1\cdot\boldsymbol{U}}=\frac{\Omega_1}{u_p} \tag{12a}$$

$$\frac{\Omega_n}{qR}=\frac{(\hat{s}\cdot\nabla\hat{s})\cdot\boldsymbol{\Omega}}{\hat{s}\cdot\boldsymbol{U}}=\frac{(\hat{i}_1\cdot\nabla\hat{i}_1)\cdot\boldsymbol{\Omega}}{\hat{i}_1\cdot\boldsymbol{U}}=\frac{\Omega_{n1}}{u_pR_1} \tag{12b}$$

where $u_p=\hat{i}_1\cdot\boldsymbol{U}_p$, $R_1$ is the principal radius of curvature of the $x_1$ coordinate, and $\Omega_{n1}$ is vorticity in the $\hat{n}_1$ direction, the principal normal of the $x_1$ coordinate. $R_1$ and $n_1$ are defined by the Frenet formula $\hat{n}_1/R_1=\hat{i}_1\cdot\nabla\hat{i}_1$; thus, in the orthogonal coordinate system used here

$$\frac{\hat{n}_1}{R_1}=-\frac{\hat{i}_2}{h_1h_2}\frac{\partial h_1}{\partial x_2} \tag{13}$$

where $h_1$ and $h_2$ are metric coefficients. Substituting $p_1$ for $p$, and taking $q^2\doteq u_p^2$ and $\hat{s}\doteq\hat{i}_1$, Eq. (11) may be approximated as

$$\tilde{u}\cdot\nabla\left(\frac{\Omega_1}{\rho u_p}\right)=\frac{2\Omega_{n1}}{\rho u_pR_1}-\frac{1}{\rho u_p^2}\hat{i}_1\cdot\nabla\times\frac{1}{\rho}\nabla p_1+\frac{\hat{i}_1}{\rho u_p^2}\cdot\boldsymbol{G}' \tag{14}$$

where $\boldsymbol{G}'$ does not contain streamwise diffusion. Finally, the normal vorticity term, $\Omega_{n1}/R_1$, is given as

$$\frac{\Omega_{n1}}{R_1}=\frac{\hat{n}_1}{R_1}\cdot\boldsymbol{\Omega}=\frac{\hat{n}_1}{R_1}\cdot\nabla\times\boldsymbol{u} \tag{15}$$

Combining the velocity decomposition equation (5) with the continuity equation, the definition of $\Omega_1$ results in

$$\nabla\cdot\rho\nabla_s\phi=-\nabla\cdot\rho\boldsymbol{u}_p \tag{16}$$

$$\hat{i}_1\cdot\nabla\times\frac{1}{\rho}\nabla\times(\hat{i}_1\psi)=\Omega_1 \tag{17}$$

Equations (16) and (17) serve to determine the scalar and vector potentials and are used in conjunction with Eqs. (3) and (14) to determine the secondary flow velocity field.

*Viscous and Heat Conduction Terms*

The viscous and heat conduction terms are approximated to suppress streamwise diffusion terms that would otherwise preclude solution by forward marching. Boundary-layer order-of-magnitude estimates are used to estimate the importance of various terms, which justifies neglecting all derivatives with respect to $x_1$ and neglecting some other terms (notably in the energy equation) to simplify the final equations. The dissipation term $\Phi$ and viscous terms involving $\nabla\cdot\boldsymbol{U}$ are also neglected, and the laminar viscosity and conductivity are assumed to be constant. Turbulent Reynolds stresses are modeled by introduction of a scalar (isotropic) effective viscosity that is added to the laminar viscosity, and the laminar and turbulent Prandtl numbers are taken as unity. The final expressions approximating the right side of Eqs. (6) and (7) and the last term in Eq. (14), respectively, are given for the orthogonal coordinates used here as

$$\hat{i}_1\cdot\boldsymbol{F}\approx\frac{\partial}{\partial y}\left[(\mu+\mu_T)\frac{h_1^2h_3}{h_2}\frac{\partial u/h_1}{\partial y}\right]+\frac{h_1h_2}{h_3}\frac{\partial}{\partial z}\left[(\mu+\mu_T)\frac{\partial u}{\partial z}\right] \tag{18}$$

$$\nabla\cdot k\nabla T+\boldsymbol{u}\cdot\boldsymbol{F}+\Phi\approx\frac{\partial}{\partial y}\left[(\mu+\mu_T)\frac{h_1h_3}{h_2}\frac{\partial E}{\partial y}\right]+\frac{h_1h_3}{h_3}\frac{\partial}{\partial z}\left[(\mu+\mu_T)\frac{\partial E}{\partial z}\right] \tag{19}$$

$$\hat{i}_1\cdot\boldsymbol{G}'\approx\left\{\frac{h_1}{h_2h_3}\frac{\partial}{\partial y}\left[\frac{h_3}{h_1h_2\rho}\frac{\partial h_1(\mu+\mu_T)\Omega_1}{\partial y}\right]+\frac{h_1}{h_3^2}\frac{\partial}{\partial z}\left[\frac{1}{\rho}\frac{\partial(\mu+\mu_T)\Omega_1}{\partial z}\right]\right\} \tag{20}$$

where $\mu_T$ is the turbulent viscosity and the metrics are independent of the azimuthal coordinate $z$.

*Turbulence Model*

Two methods of defining the scalar turbulent viscosity are considered here. In the first, the two-equation model of turbulence given by Launder and Spalding[7] for the turbulence kinetic energy $k$ and dissipation rate $\epsilon$ is used. Using Cartesian tensor notation, the turbulence kinetic energy and dissipation are conventionally defined as

$$k=\tfrac{1}{2}\overline{u_i'u_i'} \tag{21}$$

$$\epsilon=\nu\overline{\frac{\partial u_i'}{\partial x_j}\frac{\partial u_i'}{\partial x_j}} \tag{22}$$

The model transport equations for $k$ and $\epsilon$ at high Reynolds number in vector form are given in Ref. 7 as

$$\rho\boldsymbol{U}\cdot\nabla k=\nabla\cdot(\mu+\mu_T/\sigma_k)\nabla k+P-\rho\epsilon \tag{23}$$

$$\rho\boldsymbol{U}\cdot\nabla\epsilon=\nabla\cdot\left(\mu+\frac{\mu_T}{\sigma_\epsilon}\right)\nabla\epsilon+c_1\frac{\epsilon}{k}P-c_2\frac{\rho\epsilon^2}{k} \tag{24}$$

In Eqs. (23) and (24) $P$ represents the turbulence production and its approximation for the present analysis is given in Ref. 1. The quantities $\sigma_k$, $\sigma_\epsilon$, $c_1$, and $c_2$ are empirical constants assigned values of 1.0, 1.3, 1.44, and 1.92, respectively, as given in Ref. 7. From $k$ and $\epsilon$ the turbulent viscosity is obtained from the Prandtl-Kolomogrov constitutive relationship as

$$\mu_T=C_\mu\rho k^2/\epsilon \tag{25}$$

Specification of starting conditions for the turbulence quantities $k$, $\epsilon$, and $\mu_T$ is accomplished by specifying a mixing length scale $\ell$ and a freestream turbulence level, and assuming local equilibrium. The initial turbulent viscosity is then computed from $\ell$ and local velocity gradients by the conventional extension of Prandtl's mixing length to three dimensions as follows:

$$\mu_T=\rho\ell^2\left[\left(\frac{1}{h_2}\frac{\partial u}{\partial x_2}\right)^2+\left(\frac{1}{h_2}\frac{\partial w}{\partial x_2}\right)^2+\left(\frac{1}{h_3}\frac{\partial u}{\partial x_3}\right)^2+\left(\frac{1}{h_3}\frac{\partial v}{\partial x_3}\right)^2\right]^{1/2} \tag{26}$$

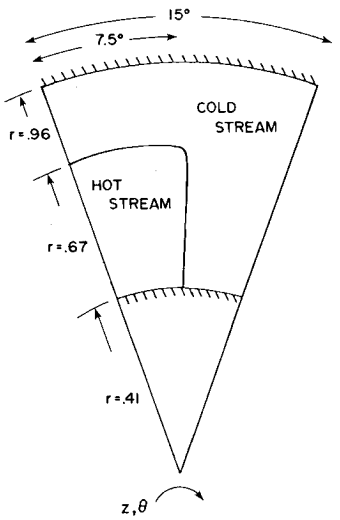


**Fig. 3 Computational segment considered in lobe mixer calculations for high-bypass configuration.**

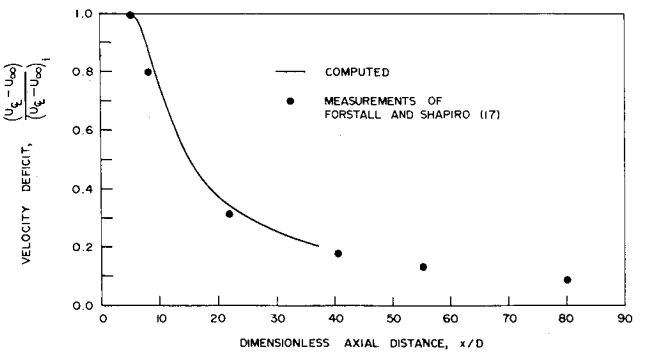


**Fig. 4 Axial decay of centerline velocity in a coaxial jet flow.**

The turbulence kinetic energy and dissipation rate are then computed from the definition of the mixing length and the Prandtl-Kolomogrov relationship as

$$k = [\mu_T / (C_\mu^{1/4} \rho \ell)]^2 \tag{27}$$

$$\epsilon = c_\mu^{3/4} k^{3/2} / \ell \tag{28}$$

Equations (27) and (28) are obtained from an assumption of local equilibrium (production equals dissipation) in conjunction with Eqs. (25) and (26). The initial $k$ distribution is corrected in the freestream and then the initial turbulent viscosity is recomputed from $k$ and $\epsilon$ using Eq. (25).

All calculations presented in the present paper employed the $k$-$\epsilon$ turbulence model, except as otherwise noted. In some other calculations using the $k$-$\epsilon$ turbulence model, negative values of dissipation occasionally have occurred, which causes a breakdown in the calculation procedure. To circumvent this difficulty if it occurs, an alternate "wake" turbulence model is considered. This much simpler model is based on the definition of turbulent viscosity $\mu_T$ and Prandtl's suggestion that the diffusional flux of some property $\phi = \bar{\phi} + \phi'$ may be expressed as

$$-\overline{v'\phi'} = \frac{1}{\sigma_\phi} k^{1/2} \ell \frac{\partial \bar{\phi}}{\partial y} = \frac{\mu_T}{\rho} \frac{\partial \bar{\phi}}{\partial y} \tag{29}$$

Hence, one obtains the Prandtl-Kolmogorov relationship

$$\mu_T = \frac{1}{\sigma_\phi} k^{1/2} \ell \rho \tag{30}$$

The wake turbulence model is obtained by assuming that the turbulent length scale and velocity scales are constant throughout the flowfield. From Eqs. (25) and (28) it follows that the constant $1/\sigma_\phi$ is simply $C_\mu^{1/4}$. The velocity scale is taken as the square root of the initially specified turbulence kinetic energy $k$. The length scale is taken as about 0.1 times the average shear layer thickness specified in the starting conditions.

*Imposed Axial Pressure Gradients*

Since the mean value of the pressure $p_v(x_1)$ is determined by the present analysis, the only influence of the imposed axial pressure gradient is in the transverse variation of this gradient from its (corrected) mean value. The effect of the imposed pressure is thus limited to the influence of the two-dimensional potential flow streamline curvature resulting from the geometry of the nozzle plug and outer casing, and this exerts only a minor influence in the flow predictions. The development of large secondary flows is governed by the streamwise vorticity equation in which the influence of the imposed pressure has essentially been eliminated. These large secondary flows originate in the lobe section upstream of the mixing duct and are introduced in the starting condition for transverse velocity and vorticity in the present analysis. In approximating the axial pressure gradients, it is important to account for the flow acceleration within the mixing duct, which is affected by viscous and mixing effects and by the axial area distribution. This aspect of the axial pressure gradient is believed to be adequately represented by the mean pressure correction $p_v(x_1)$. In light of these observations, it is believed that the imposed axial pressure gradients can be adequately represented by an incompressible axisymmetric potential flow solution that is corrected locally for compressibility effects using Laitone's variant of the Prandtl-Glauert similarity rule.[8] In the present calculation, the correction was based on the local Mach number of the viscous calculation; a cutoff value of $M = 0.7$ was imposed since this correction is inaccurate for high subsonic Mach numbers. An alternative compressibility correction for internal flows has been suggested by Lieblein and Stockman.[9] In computing this incompressible potential flow for the mixing duct geometry, uniform values of potential were specified at the upstream and downstream boundaries.

*Boundary Conditions*

Although the flow within the mixing duct is three-dimensional, the full azimuthal extent of the mixing duct need not be considered. Since the lobe geometry is periodic, only a segment of the flowfield is considered (Fig. 3) and the flow is assumed to be symmetric about $\theta_{\min}$ and $\theta_{\max}$. On the hub and casing boundaries, a wall function condition is applied to the axial velocity. This boundary condition is believed to be adequate since the mixing of the fan and turbine streams is of primary interest. This mixing takes place in free shear layers removed from near-wall regions; therefore, wall boundary layers are believed to play a minor role in the mixing process. In addition, since the wall boundary layers are not turned in a direction that would generate significant streamwise vorticity (as in a curved duct[10]), the streamwise vorticity is assumed to be zero. The boundary conditions along the hub and casing walls are given by

$$\frac{\partial u_p}{\partial x_2} = \frac{u_\tau}{\kappa x_2} \tag{31}$$

$$k = u_\tau^2 / C_\mu^{1/2} \tag{32}$$

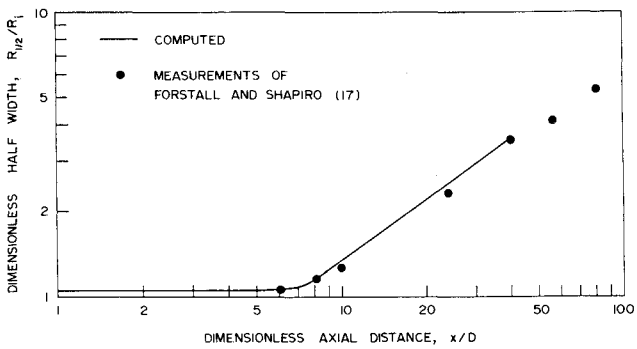


**Fig. 5 Jet spreading rate in a coaxial jet flow.**

$$\epsilon = u_\tau^3/\kappa x_2 \tag{33}$$

$$\Omega_s = 0 \tag{34}$$

$$\psi = 0 \tag{35}$$

$$\frac{\partial \phi}{\partial x_2} = 0 \tag{36}$$

In Eqs. (31-33) $u_\tau$ is the local friction velocity, $\kappa$ the von Kármán constant (0.43), and $x_2$ the distance to the nearest wall. Equations (31-33) are self-consistent and assume that a logarithmic velocity profile exists in the near-wall region. If the hub and shroud boundary layers become of more interest, these can be treated in a more rigorous manner following Ref. 10. The boundary conditions for the secondary flow variables assume that rotational secondary flows are confined to regions remote from the walls and that no through flow is permitted. Adiabatic wall conditions are applied to the thermal energy equation. The "wall" boundary conditions along the plug surface are changed to polar symmetry conditions as the calculation proceeds past the nozzle plug and on to the mixing duct centerline.

### Method of Solution

In formulating a solution algorithm for the governing equations, it is observed that linearization of the streamwise convective terms following Ref. 11 gives rise to a first-order approximation in which the convective coefficient is treated explicitly. Thus, the convective coefficients of the transverse derivatives ($v$ and $w$) may also be treated explicitly without affecting the order of the streamwise truncation error. Additionally, the velocity magnitude $\boldsymbol{U}\cdot\boldsymbol{U}$ in the gas law is approximated as $u_p^2$ as a simplification. As a result, the secondary flow equations and turbulence model equations are decoupled from the primary flow equations and these subsets may be solved sequentially. The governing equations are approximated by finite differences using two-point backward differences in the $x_1$ direction and three-point central differences for all transverse derivatives. An analytical coordinate transformation devised by Roberts[12] can be employed to introduce a nonuniform grid in each transverse direction to concentrate grid points near walls, or a hyperbolic sine transformation[13] can be used to concentrate the grid points about an arbitrary interior location within the flowfield. In either case, second-order accuracy is maintained in the transverse direction. The resulting implicit approximations to the subsets of governing equations are then sovled using efficient ADI (alternating direction implicit) and LBI (linearized block implicit) schemes.[14]

A summary of the overall algorithm used to advance the solution a single axial step follows. It is assumed that the solution is known at the $n$ level $x^n$ and is desired at the $n+1$ level $x^{n+1} = x^n + \Delta x$.

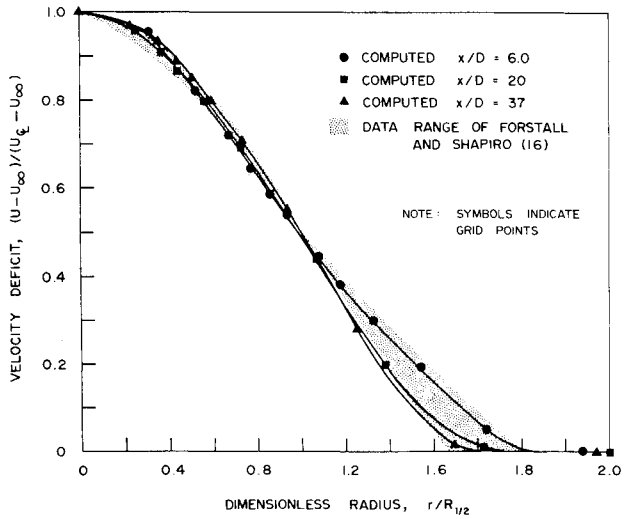


**Fig. 6 Axial velocity profiles in a coaxial jet flow.**

1) Imposed axial pressure gradients are determined from the scaled potential flow solution.

2) A value for the mean viscous pressure drop $p_v$ is assumed.

3) The momentum and energy equations are solved using a scalar ADI scheme and the density is updated algebraically using the state equation. In general, the integral mass flux constraint will not be satisfied.

4) Return to step 2 and repeat this process iteratively using the standard secant method[15] to find the value of the mean viscous pressure drop that satisfies the integral mass flux.

5) The turbulence model equations are solved using a split LBI scheme.

6) The streamwise vorticity equation is solved using a scalar ADI scheme.

7) The vector potential equation is solved using an iterative scalar ADI scheme to obtain $\psi^{n+1}$.

8) Using values now available for $\partial \rho u/\partial x$, the scalar potential equation is solved for $\phi^{n+1}$, which ensures that the composite velocity satisfies the continuity on a differential basis.

9) The secondary flow velocity components are computed from $\psi^{n+1}$ and $\phi^{n+1}$.

An automated starting procedure based on a parametric specification of the inflow conditions was used for all calculations presented here. The primary flow is described parametrically by specifying a lobe shape and mean values for both the primary flow velocity ratio and the temperature ratio between the fan and turbine streams. The primary flow velocity component is then given a cross-sectional distribution that is consistent with both this mean value and the imposed transverse pressure gradients at the initial plane, and that introduces shear layers between the fan and turbine stream. Hub and casing boundary layers may also be included if desired. The starting procedure allows the specification of nonzero secondary flow velocity components and nonzero streamwise vorticity. In the calculations reported here, this was done by prescribing two parameters that represent a mean flow angle for the fan and turbine streams. Secondary velocities are then determined from the specified flow angle and the local value of the primary flow velocity. The starting algorithm then processes these specified secondary velocity components to ensure consistency with the governing equations. First, the specified secondary velocity is differentiated to obtain the streamwise vorticity, and then the primary momentum equation is solved for one axial step. Finally, the scalar and vector potential equations are solved to obtain processed secondary flow distributions that satisfy the continuity equation and these are used as starting conditions.

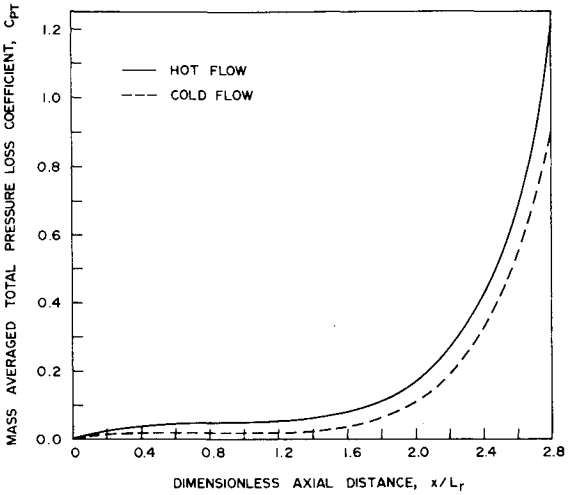


**Fig. 7 Comparison of losses for hot and cold flow in a low-bypass mixer.**

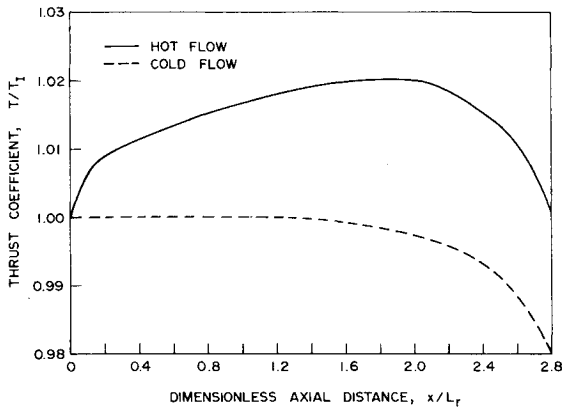


**Fig. 8 Comparison of axial thrust development for hot and cold flow in a low-bypass mixer.**

## Computed Results

### Coaxial Jet Flow

The proper operation of the solution procedure and turbulence model was first tested for a coaxial jet flow experimentally investigated by Forstall and Shapiro.[16] This flow was a test case at the NASA Langley Free Turbulent Shear Flow Conference[17] and is useful since other predictors at that conference were able to obtain good agreement with these data using the same turbulence model. Experimental measurements were obtained for a confined coaxial jet with a 16:1 radius ratio and a velocity ratio of the nozzle to outer stream of 4:1. Values of the spread rate and centerline velocity decay are given in Ref. 17 and the profile data may be found in Ref. 16.

To simplify the treatment of the starting conditions, the calculation was initiated at $X/D=1.0$ with the shear layer between the inner and outer streams modeled to match the normalized profile measured by Sami et al.[18] at $X/D=1.0$. Additional details for this case may be found in Ref. 1, where a calculation for the region $0\leq X/D<1.0$ is also presented and which shows good agreement between the predicted profile at $X/D=1.0$ and the assumed profile at $X/D=1.0$. The present calculation extended from $X/D=1.0$ to 37. Twenty grid points were used in the radial direction using a hyperbolic sine function to cluster the points in the shear layer.[1] Thirty-six axial points were used with an initial $\Delta x$ of 0.1 times the initial jet radius, increasing to 3.0 jet radii at the last station. Zero gradient conditions were specified at the centerline and outer limits of the computation.

Comparisons of the predicted and measured centerline velocity decay and jet spread rate are presented in Figs. 4 and 5, respectively. The predicted centerline velocity decay is in very good agreement with the measurements and the predicted spread rate is only slightly above the trend of the data. It should be noted that these calculations did not utilize the modifications to $c_2$ and $c_\mu$ suggested by Launder and Spalding[7] to improve the predictions of the spread rate. Recently, Janicka and Kollmann[19] also observed good agreement between predicted and measured spread rate and velocity decay using the unmodified turbulence model. Figure 6 shows the predicted streamwise velocity profiles (normalized by the jet half radius) at various $X/D$ locations and the range of data measured by Forstall. Again, the agreement is good despite a slight underresolution of the outer region at $X/D=37$, which is evident from the grid point locations in the figure.

### Lobe Mixer Flows

Several calculations of lobe mixer flows were performed to explore the potential of the method for making detailed predictions of the mixing process. The first two of these calculations were performed for a low-bypass configuration with a long mixing duct. Details of the mixer geometry for these two cases are omitted here for brevity, but may be found in Ref. 1. Both calculations were performed using 20 radial grid points, 10 azimuthal points, and 20 axial steps. One calculation was performed with uniform thermal energy in both streams and is referred to as cold flow. The other calculation was performed with different thermal energy levels in each stream and is referred to as hot flow. In both calculations, the secondary flows generated upstream of the mixing duct were omitted in the starting conditions by prescribing zero streamwise vorticity. In the hot flow case, the temperature ratio between the fan and turbine streams was 0.4 and the velocity ratio was 0.7. These conditions imply a small total pressure mismatch between the two streams, the Mach number ratio being 1.107. For the cold flow case, the same Mach number ratio and total pressure mismatch were maintained, requiring a velocity ratio of 1.107 and a temperature ratio of 1.0.

A mass-averaged total pressure loss coefficient $C_{PT}$ is defined as

$$C_{PT}=\int_A \frac{2(P_{T_{\text{ref}}}-P_T)}{(\rho u^2)_{\text{ref}}}\rho \boldsymbol{U}\cdot d\boldsymbol{A}\Big/\int_A \rho \boldsymbol{U}\cdot d\boldsymbol{A} \tag{37}$$

where $P_{T_{\text{ref}}}$, $\rho_{\text{ref}}$, and $u_{\text{ref}}$ are reference quantities associated with the turbine stream. The reference conditions are chosen to obtain $C_{PT}=0$ at the initial plane; thus, $C_{PT}$ indicates losses that occur in the mixing duct. A thrust coefficient is also defined and based on the thrust that would be obtained by isentropic expansion from local conditions to a predetermined exit pressure. The ratio of the local value of this thrust $T$ to the initial plane value $T_i$ is defined as the thrust coefficient $T/T_i$. The thrust is computed from

$$T=\int_{A_e}\gamma P_e M_e^2 dA_e \tag{38}$$

where $\gamma$ is the ratio of specific heats, $P_e$ the exit pressure, $M_e$ the Mach number based on isentropic expansion from local conditions to $P_e$, and $A_e$ the effective exit area, again based on expansion to $P_e$.

In comparing the hot and cold flow calculations, the cold flow case serves as a reference flow in which mixing duct losses not associated with thermal mixing are isolated. Differences between the hot and cold flow cases thus reflect losses and changes in thrust associated with the mixing

process. A comparison between the hot and cold flow total pressure losses is shown in Fig. 7. The hot flow exhibits higher total pressure losses, presumably due to increased viscous losses resulting from the velocity and thermal shear layers. A comparison of the thrust coefficients for the hot and cold flows is presented in Fig. 8. As expected, the cold flow shows a decrease only in thrust, since the thermal energy in both streams is initially uniform, and thus no benefit occurs from mixing. For the hot flow, a substantial gain in thrust due to thermal mixing is predicted in the region upstream of $X/L_r = 2.0$. Downstream of $X/L_r = 2.0$, the gain in thrust due to mixing is apparently more than offset by losses, resulting in a decrease in the thrust. However, the difference in thrust between the hot and cold flows at the nozzle exit is substantial and represents an overall thrust gain due to thermal mixing. This gain in thrust occurs in spite of the higher total pressure losses present in the hot flow case. These calculations thus demonstrate that predictions of improved performance due to mixing can be obtained using the present analysis.

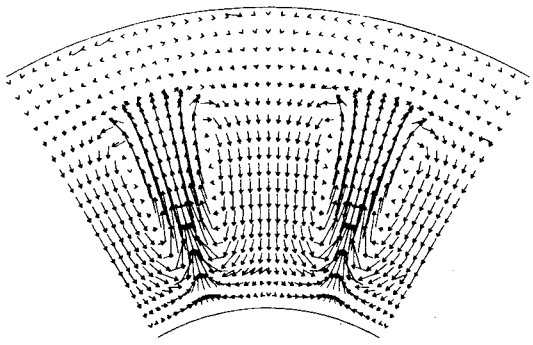

**Fig. 9 Secondary flow vectors at initial plane after processing of the parametrically specified starting vorticity.**

The influence of the secondary flows generated upstream of the mixing duct on flow within the mixing duct was explored in two additional calculations performed by Povinelli and Anderson[20,21] in collaboration with the present authors. The mixing duct geometry considered is shown in Fig. 2 and is representative of short mixing ducts used with high-bypass mixer designs. The experimental data for this configuration[20] indicates that large radial velocities are present at the lobe exit plane. The two calculations considered here differ only in whether these radial velocities and the associated streamwise vorticity are included (parametrically) or omitted in the starting conditions.

The computational segment at the initial plane for these calculations is shown in Fig. 3. The ratio of fan to turbine stream axial velocity is 0.86 and the temperature ratio is 0.74.

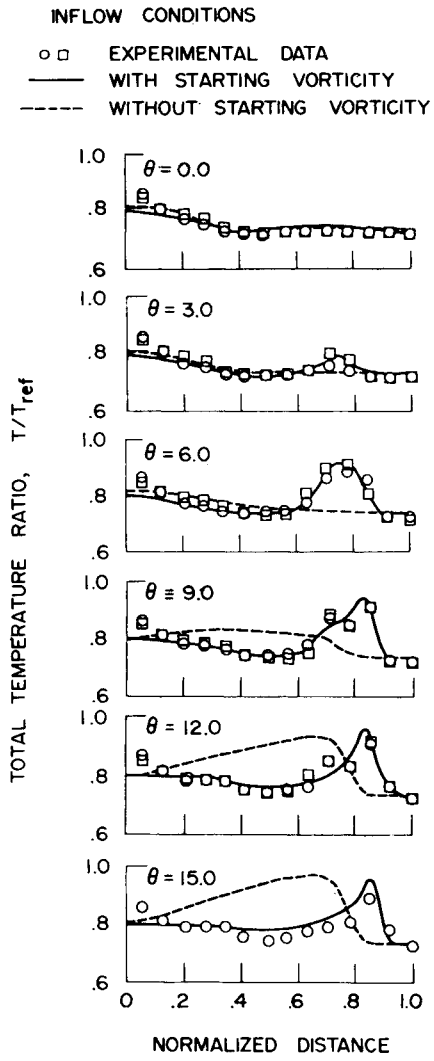


**Fig. 10 Comparison of measured and predicted total temperature distributions at nozzle exit with and without starting vorticity (high-bypass mixer).**

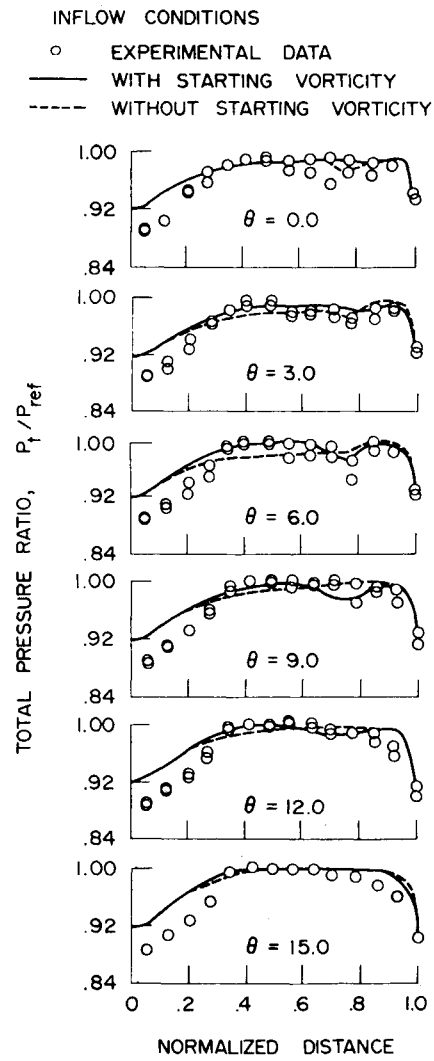


**Fig. 11 Comparison of measured and predicted total pressure profiles at nozzle exit with and without starting vorticity (high-bypass mixer).**

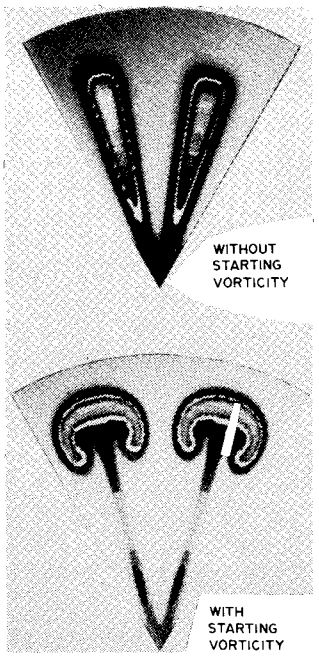


**Fig. 12 Comparison of predicted total temperature signature at nozzle exit with and without starting vorticity (high-bypass mixer).**

These conditions correspond to the matched total pressure between the fan and turbine stream with an average inlet Mach number of 0.45 and result in nearly choked flow at the nozzle exit. In one calculation, the turbine stream was given an initial radial outward velocity component of magnitude 0.25 times the local primary flow velocity and the fan stream was given a radial inflow velocity of 0.20 times the local primary flow velocity, each in accordance with the mean values observed in the experimental data. These inward fan and outward turbine radial velocities establish a large-scale vortex in the shear layer between the two streams. These initial conditions for the secondary flow velocity are shown in Fig. 9, after processing by the starting procedure. In the second calculation, the experimentally observed secondary flow present at the initial plane was neglected and zero streamwise vorticity was specified in the starting conditions. The computational mesh consisted of 40 equally spaced radial points, 10 equally spaced azimuthal points and 20 axial stations.

The total pressure predictions at the nozzle exit plane for the cases with and without starting streamwise vorticity are compared with the experimental data in Fig. 10. The total temperature predictions for both cases are compared with the data in Fig. 11. From these comparisons, it can be seen that the inlet streamwise vorticity (generated by radial deflection of the fan and turbine streams within the lobes) plays an important role in the mixing process. Additionally, the predictions with starting vorticity are in very good agreement with the experimental data, whereas the results without starting vorticity show significant qualitative as well as quantitative error. Contour plots presented in Fig. 12 show that the total temperature signature at the nozzle exit plane exhibits a "mushroom" shape, consistent with experimental observations (cf. Ref. 22), when inlet streamwise vorticity is accounted for. These comparisons indicate that the secondary flows generated by radial deflection within the mixer lobes play a significant role in the downstream flow development within the mixing duct.

A final comparison is made for two calculations that are identical except for the turbulence model ($k$-$\epsilon$ or wake) used. The flow case considered is the same as that considered in the previous comparison except the initial Mach number was

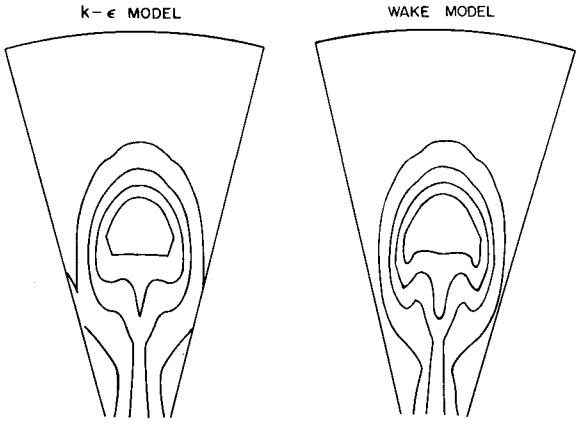


**Fig. 13 Effect of turbulence model on total temperature contours at nozzle exit (high-bypass mixer).**

0.41; the starting conditions include the secondary flow and streamwise vorticity. A comparison of total temperature contours for these calculations is given in Fig. 13 and indicates that the large-scale characteristics of the total temperature pattern are unaltered by the change in the turbulence model. Although some small-scale differences are present, the comparison indicates a pronounced lack of sensitivity to the turbulence model used.

## Conclusion

The results presented here have demonstrated that the present method can provide predictions of the total pressure losses and thrust gains associated with the mixing process. In the flows considered here, the predictions are insensitive to the turbulence model, but are sensitive to the presence of secondary flow at the lobe exit plane. Nevertheless, it appears that accurate predictions for the mixing process can be obtained using the present method provided these inlet conditions are known in sufficient detail. This type of predictive capability can be useful in a research or design study to ascertain what type of inflow conditions lead to desirable mixer performance. Knowledge of the inflow conditions thus obtained could then guide the design of the lobe sections that produce these flow conditions at the lobe exit plane. Further evaluation and implementation of the analysis and computer code, particularly in the development of the role of inlet secondary flow profiles and turbulence models in mixing and their impact on mixer design is given in a companion paper by Povinelli and Anderson.[23]

## Acknowledgment

The authors wish to acknowledge the assistance of their colleague, Dr. S.-J. Lin, who computed the solutions shown in Fig. 13.

## References

[1] Kreskovsky, J. P., Briley, W. R., and McDonald, H., "Development of a Method for Computing Three-Dimensional Subsonic Turbulent Flow in Turbofan Lobe Mixers," SRA Rept. R79-300006-F, Nov. 1979, (also NASA CR-3494).

[2] Birch, S. F., Paynter, G. C., Spalding, D. B., and Tatchell, D. G., "Numerical Modeling of Three-Dimensional Flows in Turbofan Engine Exhaust Nozzles," *Journal of Aircraft*, Vol. 15, Aug. 1978, pp. 489-496.

[3] Patankar, S. V. and Spalding, D. B., "A Calculation Procedure for Heat, Mass and Momentum Transfer in Three-Dimensional Parabolic Flows," *International Journal of Heat and Mass Transfer*, Vol. 15, Oct. 1972, pp. 1787-1806.

[4] Briley, W. R. and McDonald, H., "Analysis and Computation of Viscous Subsonic Primary and Secondary Flows," AIAA Paper 79-1453, July 1979.

[5]Anderson, O. L., "User's Manual for a Finite-Difference Calculation of Turbulent Swirling Compressible Flow in Axisymmetric Ducts with Struts and Slot Cooled Walls," USAAMRDL-TR-74-50, Vol. I, 1974.

[6]Lakshminarayana, B. and Horlock, J. H., "Generalized Expressions for Secondary Vorticity Using Intrinsic Coordinates," *Journal of Fluid Mechanics*, Vol. 59, Pt. 1, 1973, pp. 97-115.

[7]Launder, B. E. and Spalding, D. B., "The Numerical Computation of Turbulent Flows," *Computer Methods in Applied Mechanics and Engineering*, Vol. 3, April 1974, pp. 269-289.

[8]Shapiro, A. H., *The Dynamics and Thermodynamics of Compressible Fluid Flow,* Vol. I, Ronald Press, New York, 1955.

[9]Lieblein, S. and Stockman, N. O., "Compressibility Correction for Internal Flow Solutions," *Journal of Aircraft*, Vol. 9, April 1971, pp. 312-313.

[10]Kreskovsky, J. P., Briley, W. R., and McDonald, H., "Prediction of Laminar and Turbulent Primary and Secondary Flows in Strongly Curved Ducts," NASA CR-3388, Feb. 1981.

[11]Briley, W. R. and McDonald, H., "Solution of the Multidimensional Compressible Navier-Stokes Equation by a Generalized Implicit Method," *Journal of Computational Physics*, Vol. 24, Aug. 1977, pp. 372-397.

[12]Roberts, G. O., "Computational Meshes for Boundary Layer Problems," *Proceedings of the Second International Conference on Numerical Methods in Fluid Dynamics,* Springer-Verlag, New York, 1971, p. 171.

[13]Levy, R., McDonald, H., Briley, W. R., and Kreskovsky, J. P., "A Three-Dimensional Turbulent Compressible Subsonic Duct Flow Analysis for Use with Constructed Coordinate Systems," NASA CR-3389, April 1981.

[14]Briley, W. R. and McDonald, H., "On the Structure and Use of Linearized Block Implicit Schemes," *Journal of Computational Physics*, Vol. 34, Jan. 1980, pp. 54-73.

[15]Ralston, A., *A First Course in Numerical Analysis*, McGraw-Hill Book Co., New York, 1965, p. 323.

[16]Forstall, W. Jr. and Shapiro, A. H., "Momentum and Mass Transfer in Coaxial Gas Jets," *Transactions of ASME Journal of Applied Mechanics*, Vol. 17, Dec. 1950, pp. 399-408.

[17]*Free Turbulent Shear Flows, Vol. II—Summary of Data*, NASA SP-321, 1972, p. 36.

[18]Sami, S., Carmody, T., and Rouse, H., "Jet Diffusion in the Region of Flow Establishment," *Journal of Fluid Mechanics*, Vol. 27, Feb. 1967, pp. 231-252.

[19]Janicka, J. and Kollman, W., "Prediction Model for the PDF of Turbulent Temperature Fluctuations in a Heated Round Jet," *Second Symposium on Turbulent Shear Flows,* Imperial College, London, 1979, p. 1.7.

[20]Anderson, B. H., Povinelli, L A., and Gerstenmaier, W., "Influence of Pressure Driven Secondary Flows on the Behavior of Turbofan Forced Mixers," NASA TM-81541, July 1980.

[21]Povinelli, L. A., Anderson, B. H., and Gerstenmaier, W. H., "Computation of Three-Dimensional Flow in Turbofan Mixers and Comparison with Experimental Data," NASA TM-81410, Jan. 1980.

[22]Anderson, B. H. and Povinelli, L. A., "Factors Which Influence the Behavior of Turbofan Forced Mixer Nozzles," NASA TM-81668, Jan. 1981.

[23]Povinelli, L. A. and Anderson, B. H., "Investigation of Mixing in a Turbofan Exhaust Duct, Part II: Computer Code Application and Verification," *AIAA Journal*, to be published.

*From the AIAA Progress in Astronautics and Aeronautics Series . . .*

**AERO-OPTICAL PHENOMENA—v. 80**

*Edited by Keith G. Gilbert and Leonard J. Otten, Air Force Weapons Laboratory*

This volume is devoted to a systematic examination of the scientific and practical problems that can arise in adapting the new technology of laser beam transmission within the atmosphere to such uses as laser radar, laser beam communications, laser weaponry, and the developing fields of meteorological probing and laser energy transmission, among others. The articles in this book were prepared by specialists in universities, industry, and government laboratories, both military and civilian, and represent an up-to-date survey of the field.

The physical problems encountered in such seemingly straightforward applications of laser beam transmission have turned out to be unusually complex. A high intensity radiation beam traversing the atmosphere causes heat-up and breakdown of the air, changing its optical properties along the path, so that the process becomes a nonsteady interactive one. Should the path of the beam include atmospheric turbulence, the resulting nonsteady degradation obviously would affect its reception adversely. An airborne laser system unavoidably requires the beam to traverse a boundary layer or a wake, with complex consequences. These and other effects are examined theoretically and experimentally in this volume.

In each case, whereas the phenomenon of beam degradation constitutes a difficulty for the engineer, it presents the scientist with a novel experimental opportunity for meteorological or physical research and thus becomes a fruitful nuisance!

*412 pp., 6×9, illus., $30.00 Mem., $45.00 List*

TO ORDER WRITE: Publications Dept., AIAA, 555 West 57th Street, New York, N.Y. 10019